Construction of Spindle-Shaped Ti^{3+} Self-Doped TiO$_2$ Photocatalysts Using Triethanolamine-Aqueous as the Medium and Its Photoelectrochemical Properties

Zunfu Hu [1], Qi Gong [1], Jiajia Wang [1], Xiuwen Zheng [2], Aihua Wang [3] and Shanmin Gao [2,3,*]

[1] School of Materials Science and Engineering, Linyi University, Linyi 276005, China; huzunfu@lyu.edu.cn (Z.H.); gongqi72909@163.com (Q.G.); wangjiajia@lyu.edu.cn (J.W.)
[2] School of Chemistry & Chemical Engineering, Linyi University, Linyi 276005, China; zhengxiuwen@lyu.edu.cn
[3] Yantai North China Microwave Technology Co., Ltd., Yantai 264025, China; 13953598088@163.com
[*] Correspondence: gaoshanmin@lyu.edu.cn

Abstract: To enhance the utilization efficiency of visible light and reduce the recombination of photo-generated electrons and holes, spindle-shaped TiO$_2$ photocatalysts with different Ti^{3+} concentrations were fabricated by a simple solvothermal strategy using low-cost, environmentally friendly TiH$_2$ and H$_2$O$_2$ as raw materials and triethanolamine-aqueous as the medium. The photocatalytic activities of the obtained photocatalysts were investigated in the presence of visible light. X-ray diffraction (XRD), Raman spectra, transmission electron microscope (TEM), X-ray photoelectron spectroscopy (XPS), and Fourier transform infrared (FT-IR) spectra were applied to characterize the structure, morphologies, and chemical compositions of as-fabricated Ti^{3+} self-doped TiO$_2$. The concentration of triethanolamine in the mixed solvent plays a significant role on the crystallinity, morphologies, and photocatalytic activities. The electron–hole separation efficiency was found to increase with the increase in the aspect ratio of as-fabricated Ti^{3+} self-doped TiO$_2$, which was proved by transient photocurrent response and electrochemical impedance spectroscopy.

Keywords: titanium dioxide; Ti^{3+} self-doped; spindle-shaped; triethanolamine; photocatalytic

1. Introduction

As one of the most promising strategies to deal with the worldwide environmental and energy crises, photocatalytic (PC) technology takes particular attention of being a green technology that can be applied under solar conditions. PC activity is largely determined by the separation efficiency of photogenerated electrons and holes with high chemical energy [1,2]. Due to its earth abundance, nontoxic high-photoelectrical conversion performance [3], and strong chemical stability against photo and chemical corrosion, TiO$_2$ has been extensively applied as photocatalyst for solar hydrogen production [4], photovoltaic power generation [5,6], sewage purification [7–9], air purification, and other fields [10,11]. Hence, TiO$_2$-based photocatalysts with high PC activity have received continuous attention. However, two defects, wide band-gap (3.2 eV for pure TiO$_2$) and rapid charge recombination rate, limit the large-scale application of TiO$_2$-based photocatalysts [12,13]. Hence, PC activity may be enhanced by comprehensive studies on band engineering and charge carrier dynamics to solve the above problems of pure TiO$_2$ photocatalyst [14,15].

Many strategies have been developed during the past few decades to enhance the absorption of visible light [1,16]. Heteroatom doping is the most basic way of changing the electronic structure of functional materials; for instance C [17], S [18,19], and N doping [20,21], acting as electronic donation, and receipt have long been actively used to modify wide band-gap TiO$_2$ photocatalysts for visible light absorption. In addition, surface modification strategies also were applied to improve the PC activity of TiO$_2$, such as transition

metal doping, dye sensitization, inorganic combination, and nanostructure-tuning [22]. These efforts usually suffer from the leakage of harmful metal ions, thermal instability, and the increase in deleterious recombination centers for photogenerated charges [23–26]. These vital drawbacks have increased the limited use of TiO_2-based materials in developing photocatalysts. Therefore, reasonable modification strategies play a major role in improving PC properties of TiO_2-based photocatalysts.

As a typical n-type semiconductor, TiO_2 possesses intrinsic oxygen deficiency. The introduction of Ti^{3+} and oxygen vacancies (OVs) was employed to broaden the visible light absorption range and promote the charge separation [13,27,28]. Hence, Ti^{3+} self-doped TiO_2 nanomaterials have been widely investigated for their extended visible light absorption and high conductivity [29,30]. Inducting Ti^{3+} and OVs would create new defect states below the conduction band of TiO_2, thus increasing its PC activity [31–34]. Thus far, various strategies for introducing Ti^{3+} are often used; examples are thermal annealing at a high temperature in various reducing atmospheres, such as H_2, CO, H_2/Ar, or vacuum [35–37]. Nevertheless, the above strategies face the problems of high equipment requirements and high manufacturing costs. Hence, developing a facile strategy to construct Ti^{3+} self-doped TiO_2 is still a potential research topic.

Bulk and surface studies cannot elucidate the shape dependence effect, which is regarded as the origin of the higher performance of smaller particles. Serial organic surfactants, such as PVP [38], PEG [39], CTAB [40], thiophenol [41], and TEA [42] have been employed to tune the size and morphology and to prevent agglomeration. The introduction of surfactant could also stabilize the active adsorption sites that are conducive to the formation of smaller TiO_2-based photocatalysts [43,44]. In our previous work, reduced TiO_2 photocatalysts with different OVs contents were prepared by hydrothermal method, and the effects of hydrothermal treatment temperature and time consumed on the structure, morphology, and properties of the obtained samples were studied [45,46]. However, the solvent effect has an important impact on the morphology of the product, thus affecting the PC performance of the products. As a soluble, inexpensive, and readily available organic surfactant, triethanolamine ($N(CH_2CH_2OH)_3$, TEA) plays a vital role in the regulation of crystallinity, morphology, and electronic structure of the TiO_2-based photocatalysts [47–53]. Herein, to optimize the PC performance of TiO_2, a facile mixed solvothermal method was developed to fabricate spindle-shaped Ti^{3+} self-doped TiO_2 with TEA as structure-directing and capping agent.

2. Construction of Spindle-Shaped TiO_2 Photocatalysts with Ti^{3+} and OVs

Ti^{3+} self-doped TiO_2 photocatalysts were prepared with TiH_2 as Ti source, H_2O_2 as oxidant, and TEA as structure-directing agent. The entire synthesis process is illustrated in Scheme 1. The sol obtained by oxidizing TiH_2 with H_2O_2 was evenly divided into five parts, and then different amounts of TEA and H_2O were added, respectively. The solvothermal reaction subsequently was conducted at 180 °C for 20 h. The products were cleaned with deionized water and absolute ethanol three times, and centrifugate was collected. After drying at 60 °C, light blue photocatalysts were obtained.

The chemicals, detailed preparation process, characterization, PC, and photoelectro-chemical measurement experiment of the spindle-shaped TiO_2 with Ti^{3+} self-doped are detailed in the Supplementary Materials.
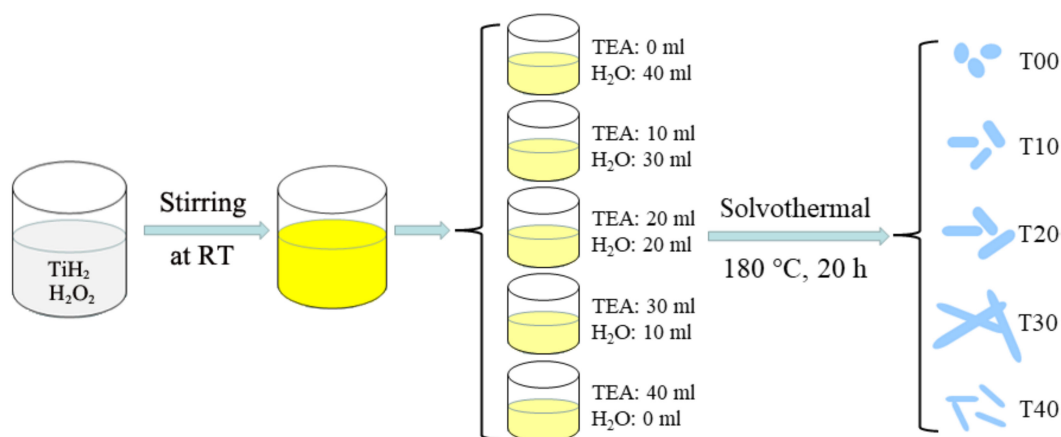
Scheme 1. Schematic diagram of the synthesis route of Ti^{3+} self-doped TiO_2 photocatalysts.

3. Results and Discussion

Ti^{3+} self-doped TiO_2 nanoparticles were prepared with different concentrations of TEA (0, 10, 20, 30, and 40 mL) via the solvothermal method at 180 °C for 20 h. The corresponding TiO_2 nanoparticles were denoted as T00, T10, T20, T30, and T40, respectively. The morphology, structure, and composition of nanomaterials are known to have a direct impact on their PC performance. X-ray diffraction (XRD) was applied to study the structure and crystallization of obtained photocatalysts. As depicted in Figure 1a, those peaks located at 25.3°, 37.9°, 48.0°, 54.1°, 54.9°, 62.7°, and 68.9° represented the (101), (004), (200), (105), (211), (204), and (216) crystal planes of pure TiO_2, maintaining the standard card of anatase TiO_2 (JCPDS No. 21–1272) [16,54]. The peaks of TiH_2 were not found in the XRD results, which proved that TiH_2 was converted into anatase TiO_2. Furthermore, with the increase in TEA content from 10 to 40 mL, the intensities of diffraction peaks decreased gradually, suggesting a decreased crystallinity for TiO_2. It might be attributed to the formation of defects with high content of TEA (Figure 1b). With the increase in TEA amount, the half-width was gradually increasing, indicating that the crystallinity of the sample was deteriorated. The above XRD results show that the content of TEA had a direct effect on the crystallinity of TiO_2 photocatalysts.
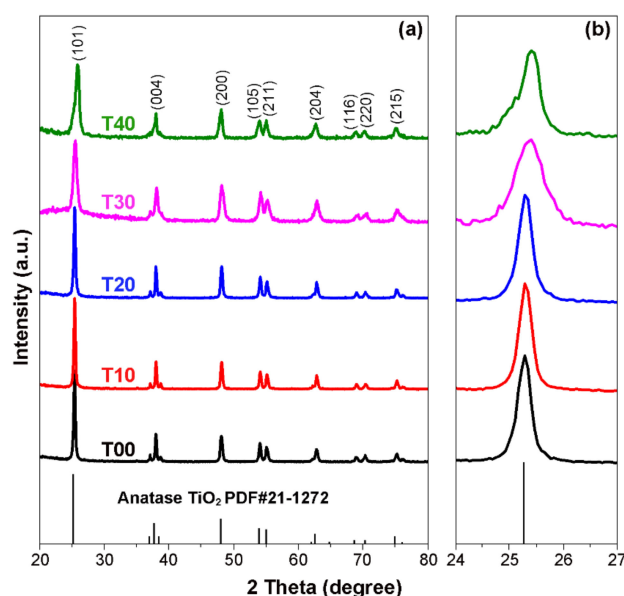

Figure 1. (**a**) XRD spectra of TiO_2 photocatalysts obtained by solvothermal treatment of the sol at different triethanolamine concentrations and (**b**) enlarged XRD results.

As a simple, effective, and high-sensitivity detection technology, Raman spectra, originating from the vibration of molecular bonds, were employed to explore the significant structural changes in TiO_2. As shown in Figure 2a, these peaks located at 145, 398, 514, and 636 cm^{-1} could index, respectively, to Eg, B1g, A1g, and Eg lattice vibration modes, indicating that all these nanomaterials were mainly anatase TiO_2 [55]. As illustrated in Figure 2b, the strongest Raman bands around 145 cm^{-1} shifted to a lower wavenumber along with the peak broadening as the content of TEA increased from 10 to 40 mL, which might be attributed to the increase in the aspect ratio of spindle-shaped TiO_2 nanoparticles. At the same time, the shift and broadening content reached the highest with 40 mL TEA, indicating that there existed a large number of defects in T40.
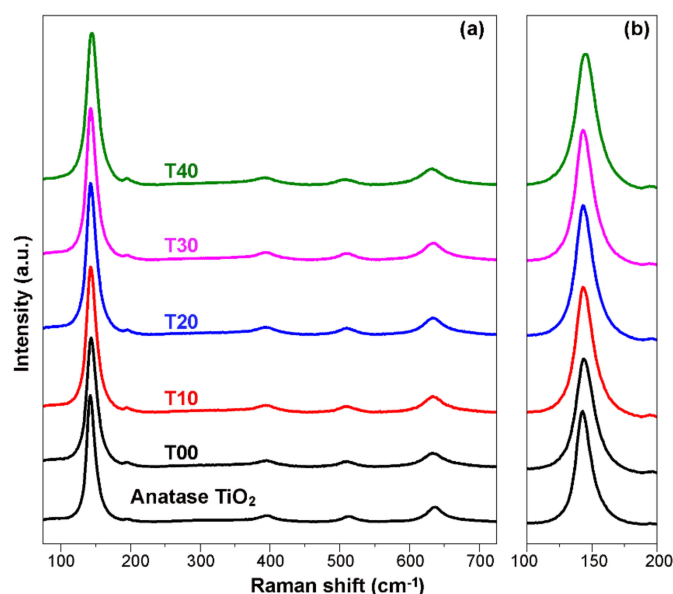

Figure 2. (**a**) Raman spectra of TiO_2 photocatalysts obtained by hydrothermal treatment the sol at different triethanolamine concentrations and (**b**) enlarged Raman results.

Transmission electron microscopy (TEM) and HRTEM were employed to investigate the representative microstructures and crystalline properties of as-prepared nanomaterials. As shown in Figure 3, as-obtained samples were spindle-shaped particles. It was easy to find that the TEA concentration in the medium significantly affected the morphology of TiO_2 nanomaterials. In absence of TEA, the obtained nanomaterials were a spherical-like particle (Figure S1a,b). The morphologies of as-obtained TiO_2 nanomaterials become spindle-shaped in the presence of TEA. With the increase in TEA amount, the spindle-shaped nanorods became narrower and longer (Figure 3a–c). However, when the amount of TEA reached to 40 mL, the obtained sample become fragmented (Figure 3e), which further indicated that the amount of TEA had an important effect on the morphology of the TiO_2 nanomaterials. The HRTEM results demonstrated that the crystallinity of the TiO_2 photocatalysts decreased gradually with the increase in TEA (Figures 3d,f and S1c,d). The crystal lattices of T00 were measured at 0.351 nm), which matched the (101) crystal plane of anatase TiO_2. While with increase in TEA, the crystal lattices of T10, T20, T30, and T40 decreased from 0.351 nm to 0.346 nm (Figures S1c,d and 3d,f), indicating that the modification of TEA would affect the crystallinity of TiO_2 nanomaterials.
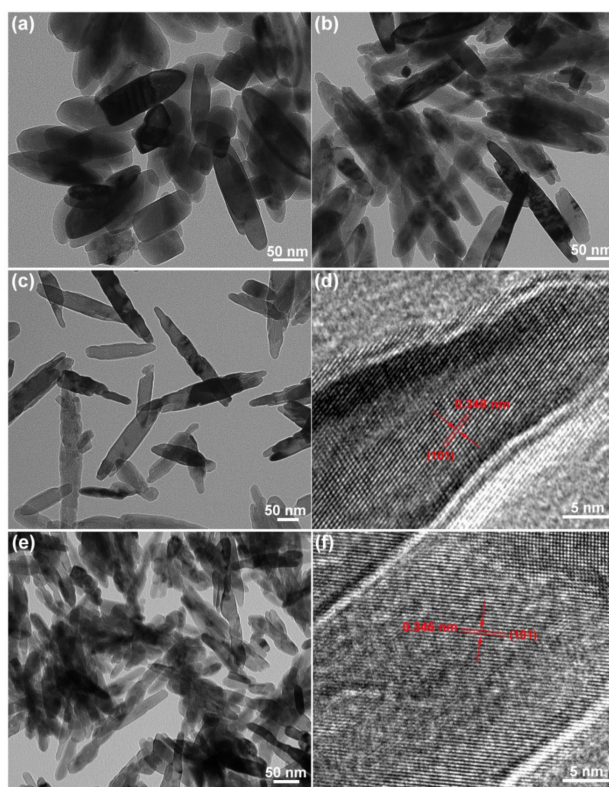
Figure 3. TEM and HRTEM pictures of TiO_2 photocatalysts obtained with different content of TEA: (**a**) T10, (**b**) T20, (**c,d**) T30, and (**e,f**) T40.

The XPS analysis is applied to further study the surface chemical environment of as-obtained TiO_2 photocatalysts. The survey XPS patterns showed that as-fabricated TiO_2 photocatalysts all contain O, C, and Ti (Figure S2). With the increase in TEA amounts in the medium, the N element binding energy peak appeared, indicating that the product contains N element on its surface. As illustrated in Figure 4a, the high-resolution XPS spectrum of Ti 2p for T00, T40 showed two peaks, which can be fitted into four peaks at 457.9, 458.6, 463.4, and 464.3 eV, assigning to Ti^{3+} $2p_{3/2}$, Ti^{4+} $2p_{3/2}$, Ti^{3+} $2p_{1/2}$, and Ti^{4+} $2p_{1/2}$, respectively [56,57]. Similarly, the XPS spectrum of O 1s for T00 and T40 also showed two peaks, which can be fitted into three peaks at 529.6, 530.5, and 532.2 eV, assigning to Ti–O bond, O–H, and OVs [58,59]. Compared with T00, the content of Ti^{3+} and OVs in the sample with TEA was greatly increased, indicating that the addition of TEA could not only form a one-dimensional spindle product but also regulate the content of Ti^{3+} and OVs in the product. Through comparative analysis of the binding energy peaks of Ti^{3+} $2p_{3/2}$ in all obtained samples, the content of Ti^{3+} was found to increase with the increase in TEA amount in the mixed solvent, which further demonstrated the influence of solvent effect on the product composition (Supporting Information, Figure S3). On one hand, a one-dimensional structure was conducive to the separation of photogenerated electrons and holes [55]. On the other hand, the introduction of Ti^{3+}/OVs could lower the band-gap of TiO_2, which facilitated the application of visible light and the improvement of PC performance. The C 1s spectra of T00, shown in Figure 4c, was deconvolved into one peak located at 284.7 eV, assigning to the C–C bond with sp^2 orbital [60]. As comparison, C 1s spectra of T20 were fitted into two peaks at 284.7 and 288.5 eV, the latter of which was assigned as C–N bond. Similarly, the C 1s spectra of T40 were deconvolved into three peaks at 284.7, 286.1, and 288.5 eV, among which the peak at 286.1 eV was assigned to C–H with sp^3 hybridization, indicating the introduction of TEA. Moreover, high-resolution N 1s spectra of T20 and T40 showed one more peak at 399.8 eV compared to the N 1s spectra of T00, which was assigned to the C–N–C bond (Figure 4d), further confirming

the introduction of TEA on the surface of TiO_2. A binding energy peak of Ti–C or Ti–N bond was not in all samples, which indicated that the C or N doping is not formed during the solvothermal treatment, and TEA only attached to the surface of TiO_2 by physical adsorption. In addition, the FT-IR analysis results also proved that TEA anchored onto TiO_2 photocatalysts (Supporting Information, Figure S4).
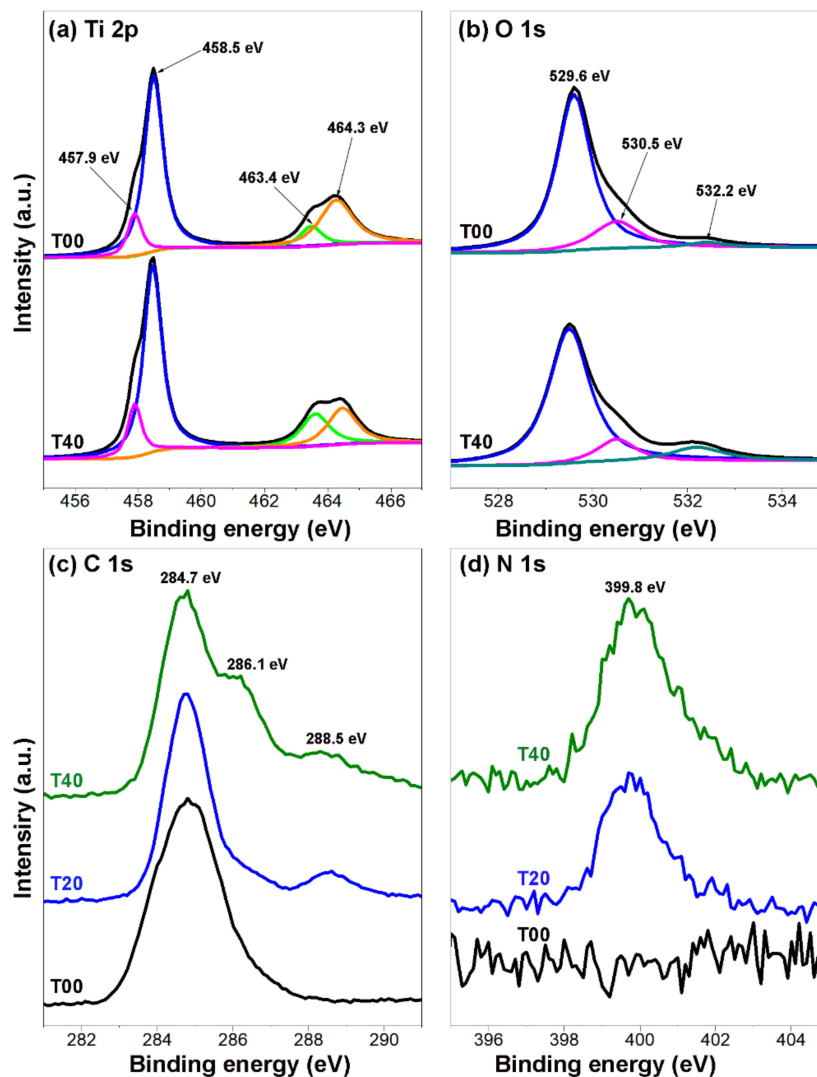

Figure 4. High-resolution XPS spectrum of different samples.

The optical performance of as-fabricated TiO_2 photocatalysts was investigated by UV-vis diffuse reflectance spectra (DRS). As illustrated in Figure 5a, with TEA as a structure-directing and capping agent, the photo-response performance of TiO_2 photocatalysts was greatly improved, extending to visible and infrared light regions. Furthermore, T40 exhibited the highest UV-vis absorption property than the other samples, indicating that the introduction Ti^{3+}/OVs could produce a novel vacancy band located below the conduction band edge of anatase TiO_2. As illustrated in Figure 5b, the band-gap energy of T40 was calculated to be 2.93 eV via plotting Kubelka–Munk formula against the photon energy. The band energy of T30, T20, T10, T00, and anatase TiO_2 were calculated to be 3.00, 3.03, 3.08, 3.05, and 3.12 eV, which were larger than that of T40.
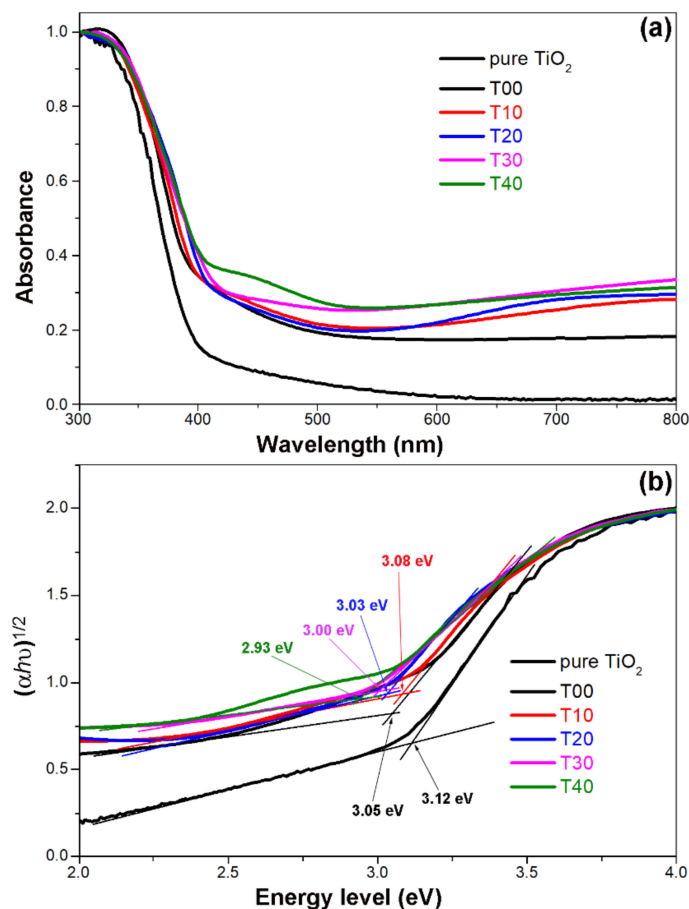
Figure 5. (**a**) UV-vis diffuse reflectance spectrum of TiO_2 photocatalysts; (**b**) Plotting curves of Kubelka–Munk against photon energy over pure TiO_2, T00, T10, T20, T30 and T40, respectively.

Photoelectrochemical transient photocurrent response under visible light can feasibly investigate the photogenerated electrons transfer property [61]. The instantaneous photocurrent data of those photocatalysts were investigated under visible light irradiation at an interval of 50 s. As displayed in Figure 6a, the photocurrent density of T10 was measured as 1.3 $\mu A\ cm^{-2}$, while that of T20 and T30 were 2.8 and 3.6 $\mu A\ cm^{-2}$, respectively. The photocurrent disappeared immediately after the visible light was removed, indicating that the photocurrent was completely generated by the photoelectrodes. Charge separation and transfer of photocatalysts were obtained by electrochemical impedance spectroscopy [62]. Figure 6b shows that the radius of the arch for T30 was smallest among those prepared TiO_2 photocatalysts, indicating that T30 exhibited the lowest impedance. The above experimental results showed that Ti^{3+} self-doped and spindle structure were beneficial to the separation and transfer efficiency of photogenerated electron-holes.

The PC performance of as-prepared TiO_2 photocatalysts was investigated by the degradation of Rhodamine B (RhB) when exposed to visible light. The time-dependent curve of concentration and spectrum during RhB degradation is shown in Figure 7a. Figure 7a also shows that the photodegradation of RhB dyes was not observed without photocatalyst. This indicates that RhB cannot be degraded under visible light while T30 sample showed the strongest PC activity, which was mainly attributed to its aspect ratio, allowing the generation of photogenerated electrons and holes and electron transfer to the surface. The stability of photocatalyst had an important influence on its practical application. Recycling experiment was employed to investigate the stability of as-prepared photocatalysts. As illustrated in Figure 7b, after six cycles, the PC performance of T30 had almost no loss, indicating that as-obtained possessed high PC stability and high practical application had potential.
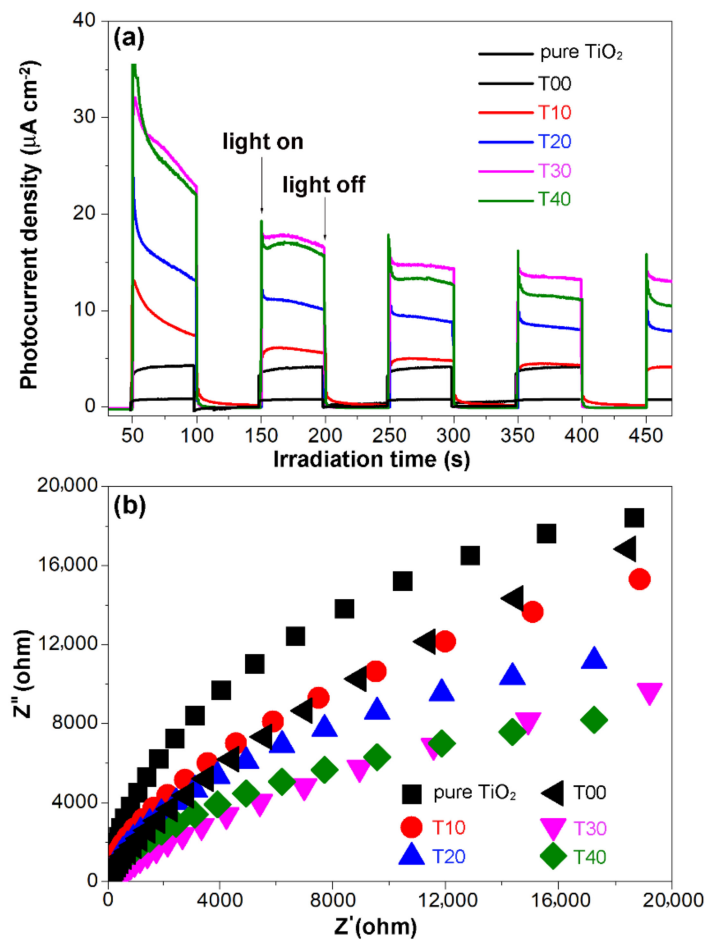
Figure 6. Transient photocurrent response (**a**) and EIS spectrum (**b**) of Nyquist plots acquired at open-circuit potential exposed to visible light illumination for different samples.
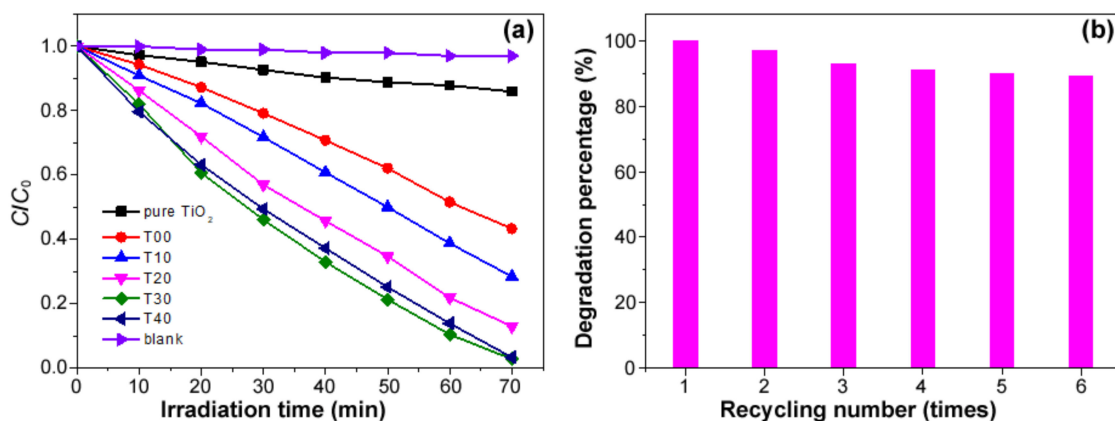

Figure 7. (**a**) Photocatalytic performance of the different samples; (**b**) recyclability of T30 in degradation of Rhodamine B.

Generally, the PC activity is determined directly by the separation efficiency of photogenerated electrons and holes. In addition, it is widely recognized that photocatalysts with a larger specific surface can supply more surface active sites for the adsorption of RhB molecules, resulting in an enhanced PC performance. The BET surface results show that T00 sample has the largest surface area, while T30 sample has the smallest surface (Supporting Information, Figure S5); however, T30 has the best PC performance, which indicates that the specific surface areas are not the main factor affecting the PC performance. In addition,

Figure 6 shows that T30 sample has the largest photocurrent and the smallest impedance, indicating that T30 has the higher separation effect of photogenerated electrons and holes. Therefore, the enhanced PC activity of Ti^{3+} self-doped TiO_2 photocatalysts is attributed to the following reasons: (i) The introduction of Ti^{3+}/OVs defects are used to reduce the band-gap of TiO_2 into the visible light range and subsequently the new defect states appear below conduction band, and (ii) the spindle-shaped nanoparticles are beneficial to the separation of photogenerated electron holes and electron transport [55]. In addition, the introduction of Ti^{3+}/OVs enhances the charge separation and diffusion while suppressing charge carrier recombination. When exposed to visible light, photogenerated electrons could change from valence band to conduction band, promoting the migration of electrons and holes to the surface TiO_2 nanoparticles. As displayed in Figure 8, photogenerated electrons react with dissolved O_2 to produce superoxide anion radicals ($\bullet O_2^-$), while holes oxidize the surface OH^- groups and H_2O molecules to generate $\bullet OH$. The highly reductive $\bullet O_2^-$ and oxidizing $\bullet OH$ will decompose RhB molecules into small micromolecules, such as H_2O and CO_2. Nevertheless, excessive Ti^{3+} would lead to the formation of the recombination center for photogenerated electron–hole pairs, which were harmful to the improvement of photocatalytic performance of TiO_2.
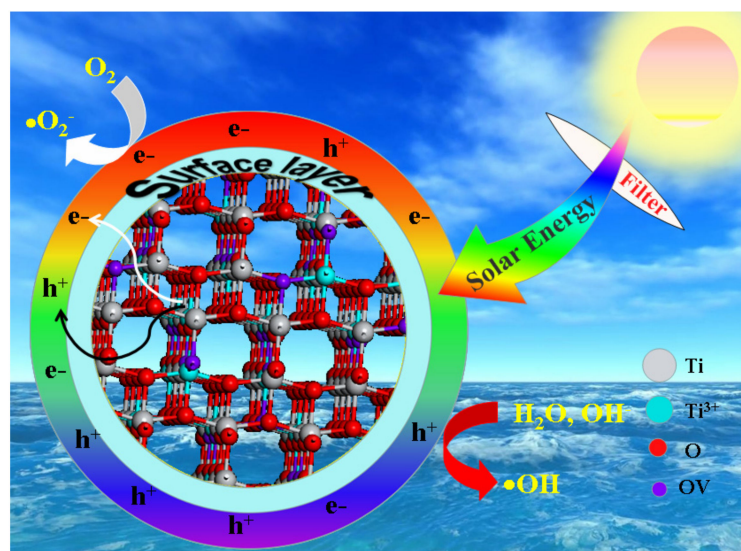

Figure 8. Schematic illustration of the visible-light photocatalytic mechanism of the Ti^{3+} self-doped TiO_2 nanoparticles.

4. Conclusions

In conclusion, spindle-shaped Ti^{3+} self-doped TiO_2 photocatalysts were fabricated by a simple solvothermal strategy with triethanolamine as a structure-directing agent. The morphology and photochemical properties of TiO_2 photocatalysts could be effectively controlled by adjusting the amount of trimethylamine. In addition, the crystallinity, photogenerated electrons, and holes of the TiO_2 catalysts could also be effectively controlled by changing the amount of trimethylamine. As-prepared TiO_2 photocatalysts were also employed for the photocatalytic degradation of rhodamine B. It was found that T30 exhibited the highest catalytic efficiency, which was mainly due to the large aspect ratio. Hence, the Ti^{3+} self-doped TiO_2 photocatalysts with large aspect ratio will be a feasible alternative strategy for water treatment and organic degradation in the future.

tained samples with different TEA amount; Figure S5: N$_2$ adsorption-desorption isotherms and the corresponding BET surface area of the different samples.

Institutional Review Board Statement: Not applicable.

Informed Consent Statement: Not applicable.

Data Availability Statement: Data presented in this article are available at request from the corresponding author.

References

1. Kang, X.; Song, X.Z.; Han, Y.; Cao, J.; Tan, Z. Defect-engineered TiO$_2$ Hollow Spiny Nanocubes for Phenol Degradation under Visible Light Irradiation. *Sci. Rep.* **2018**, *8*, 5904. [CrossRef] [PubMed]
2. Fang, L.; Chen, J.; Zhang, M.; Jiang, X.; Sun, Z. Introduction of Ti^{3+} ions into heterostructured TiO$_2$ nanotree arrays for enhanced photoelectrochemical performance. *Appl. Surf. Sci.* **2019**, *490*, 1–6. [CrossRef]
3. Ma, X.; Wang, C.; Wu, F.; Guan, Y.; Xu, G. TiO$_2$ nanomaterials in photoelectrochemical and electrochemiluminescent biosensing. *Top. Curr. Chem.* **2020**, *378*, 28. [CrossRef] [PubMed]
4. Li, J.; Cushing, S.K.; Zheng, P.; Senty, T.; Meng, F.; Bristow, A.D.; Manivannan, A.; Wu, N. Solar hydrogen generation by a CdS-Au-TiO$_2$ sandwich nanorod array enhanced with Au nanoparticle as electron relay and plasmonic photosensitizer. *J. Am. Chem. Soc.* **2014**, *136*, 8438–8449. [CrossRef]
5. Pradhan, S.C.; Velore, J.; Hagfeldt, A.; Soman, S. Probing photovoltaic performance in copper electrolyte dye-sensitized solar cells of variable TiO$_2$ particle size using comprehensive interfacial analysis. *J. Mater. Chem. C* **2022**, *10*, 3929–3936. [CrossRef]
6. Xiu, Z.; Guo, M.; Zhao, T.; Pan, K.; Xing, Z.; Li, Z.; Zhou, W. Recent advances in Ti^{3+} self-doped nanostructured TiO$_2$ visible light photocatalysts for environmental and energy applications. *Chem. Eng. J.* **2020**, *382*, 123011. [CrossRef]
7. Deng, X.; Zhang, H.; Guo, R.; Ma, Q.; Cui, Y.; Cheng, X.; Xie, M.; Cheng, Q. Effect of Ti^{3+} on enhancing photocatalytic and photoelectrochemical properties of TiO$_2$ nanorods/nanosheets photoelectrode. *Sep. Purif. Technol.* **2018**, *192*, 329–339. [CrossRef]
8. Cheng, D.; Li, Y.; Yang, L.; Luo, S.; Yang, L.; Luo, X.; Luo, Y.; Li, T.; Gao, J.; Dionysiou, D.D. One-step reductive synthesis of Ti^{3+} self-doped elongated anatase TiO$_2$ nanowires combined with reduced graphene oxide for adsorbing and degrading waste engine oil. *J. Hazard. Mater.* **2019**, *378*, 120752. [CrossRef]
9. Hao, W.; Li, X.; Qin, L.; Han, S.; Kang, S.-Z. Facile preparation of Ti^{3+} self-doped TiO$_2$ nanoparticles and their dramatic visible photocatalytic activity for the fast treatment of highly concentrated Cr(vi) effluent. *Catal. Sci. Technol.* **2019**, *9*, 2523–2531. [CrossRef]
10. Wajid Shah, M.; Zhu, Y.; Fan, X.; Zhao, J.; Li, Y.; Asim, S.; Wang, C. Facile Synthesis of Defective TiO$_{2-x}$ Nanocrystals with High Surface Area and Tailoring Bandgap for Visible-light Photocatalysis. *Sci. Rep.* **2015**, *5*, 15804. [CrossRef]
11. Liu, G.; Han, K.; Ye, H.; Zhu, C.; Gao, Y.; Liu, Y.; Zhou, Y. Graphene oxide/triethanolamine modified titanate nanowires as photocatalytic membrane for water treatment. *Chem. Eng. J.* **2017**, *320*, 74–80. [CrossRef]
12. Cai, J.; Huang, Z.a.; Lv, K.; Sun, J.; Deng, K. Ti powder-assisted synthesis of Ti^{3+} self-doped TiO$_2$ nanosheets with enhanced visible-light photoactivity. *RSC Adv.* **2014**, *4*, 19588–19593. [CrossRef]
13. Xing, H.; Wen, W.; Wu, J.-M. Enhanced UV photoactivity of Ti^{3+} self-doped anatase TiO$_2$ single crystals hydrothermally synthesized using Ti-H$_2$O$_2$-HF reactants. *J. Photochem. Photobiol. A Chem.* **2019**, *382*, 111958. [CrossRef]
14. Naldoni, A.; Altomare, M.; Zoppellaro, G.; Liu, N.; Kment, S.; Zboril, R.; Schmuki, P. Photocatalysis with Reduced TiO$_2$: From Black TiO$_2$ to Cocatalyst-Free Hydrogen Production. *ACS Catal.* **2019**, *9*, 345–364. [CrossRef] [PubMed]
15. Yin, G.; Huang, X.; Chen, T.; Zhao, W.; Bi, Q.; Xu, J.; Han, Y.; Huang, F. Hydrogenated Blue Titania for Efficient Solar to Chemical Conversions: Preparation, Characterization, and Reaction Mechanism of CO$_2$ Reduction. *ACS Catal.* **2018**, *8*, 1009–1017. [CrossRef]
16. Hamisu, A.; Gaya, U.I.; Abdullah, A.H. Bi-template assisted sol-gel synthesis of photocatalytically-active mesoporous anatase TiO$_2$ nanoparticles. *Appl. Sci. Eng. Prog.* **2021**, *14*, 313–327. [CrossRef]
17. Wang, Y.; Sun, L.; Chudal, L.; Pandey, N.K.; Zhang, M.; Chen, W. Fabrication of Ti^{3+} Self-doped TiO$_2$ via a Facile Carbothermal Reduction with Enhanced Photodegradation Activities. *ChemistrySelect* **2019**, *4*, 14103–14110. [CrossRef]

18. Li, M.; Xing, Z.; Jiang, J.; Li, Z.; Kuang, J.; Yin, J.; Wan, N.; Zhu, Q.; Zhou, W. In-situ Ti^{3+}/S doped high thermostable anatase TiO_2 nanorods as efficient visible-light-driven photocatalysts. *Mater. Chem. Phys.* **2018**, *219*, 303–310. [CrossRef]

19. Huang, Z.; Gao, Z.; Gao, S.; Wang, Q.; Wang, Z.; Huang, B.; Dai, Y. Facile synthesis of S-doped reduced TiO_{2-x} with enhanced visible-light photocatalytic performance. *Chin. J. Catal.* **2017**, *38*, 821–830. [CrossRef]

20. Sun, M.; Yao, Y.; Ding, W.; Anandan, S. N/Ti^{3+} co-doping biphasic TiO_2/Bi_2WO_6 heterojunctions: Hydrothermal fabrication and sonophotocatalytic degradation of organic pollutants. *J. Alloy. Compd.* **2020**, *820*, 153172. [CrossRef]

21. Cao, Y.; Xing, Z.; Shen, Y.; Li, Z.; Wu, X.; Yan, X.; Zou, J.; Yang, S.; Zhou, W. Mesoporous black Ti^{3+}/N-TiO_2 spheres for efficient visible-light-driven photocatalytic performance. *Chem. Eng. J.* **2017**, *325*, 199–207. [CrossRef]

22. Qiao, M.; Wu, S.; Chen, Q.; Shen, J. Novel triethanolamine assisted sol–gel synthesis of N-doped TiO_2 hollow spheres. *Mater. Lett.* **2010**, *64*, 1398–1400. [CrossRef]

23. Si, L.; Huang, Z.; Lv, K.; Tang, D.; Yang, C. Facile preparation of Ti^{3+} self-doped TiO_2 nanosheets with dominant {001} facets using zinc powder as reductant. *J. Alloy. Compd.* **2014**, *601*, 88–93. [CrossRef]

24. Pan, Y.; Wen, M. Noble metals enhanced catalytic activity of anatase TiO_2 for hydrogen evolution reaction. *Int. J. Hydrog. Energy* **2018**, *43*, 22055–22063. [CrossRef]

25. Wang, L.; Luo, H.; Zhou, X.; Wei, A.; Zhou, K.; Chen, Z.; Zhang, D. Enhanced permittivity and energy density of P (VDF-HFP)-based capacitor using core-shell structured $BaTiO_3$@TiO_2 fillers. *Ionics* **2018**, *24*, 3975–3982. [CrossRef]

26. Wang, J.; Wang, X.; Yan, J.; Tan, Q.; Liang, G.; Qu, S.; Zhong, Z. Enhanced Photoelectrochemical Properties of Ti^{3+} Self-Doped Branched TiO_2 Nanorod Arrays with Visible Light Absorption. *Materials* **2018**, *11*, 1971. [CrossRef]

27. Li, Y.; Ye, X.; Cao, S.; Yang, C.; Wang, Y.; Ye, J. Oxygen-Deficient Dumbbell-Shaped Anatase TiO_{2-x} Mesocrystals with Nearly 100% Exposed {101} Facets: Synthesis, Growth Mechanism, and Photocatalytic Performance. *Chem. A Eur. J.* **2019**, *25*, 3032–3041. [CrossRef]

28. Kuang, J.; Xing, Z.; Yin, J.; Li, Z.; Tan, S.; Li, M.; Jiang, J.; Zhu, Q.; Zhou, W. Ti^{3+} self-doped rutile/anatase/TiO_2(B) mixed-crystal tri-phase heterojunctions as effective visible-light-driven photocatalysts. *Arab. J. Chem.* **2020**, *13*, 25682578. [CrossRef]

29. Zhang, X.; Hu, W.; Zhang, K.; Wang, J.; Sun, B.; Li, H.; Qiao, P.; Wang, L.; Zhou, W. Ti^{3+} Self-Doped Black TiO_2 Nanotubes with Mesoporous Nanosheet Architecture as Efficient Solar-Driven Hydrogen Evolution Photocatalysts. *ACS Sustain. Chem. Eng.* **2017**, *5*, 6894–6901. [CrossRef]

30. Ren, R.; Wen, Z.; Cui, S.; Hou, Y.; Guo, X.; Chen, J. Controllable Synthesis and Tunable Photocatalytic Properties of Ti^{3+}-doped TiO_2. *Sci. Rep.* **2015**, *5*, 10714. [CrossRef]

31. Kang, X.; Liu, S.; Dai, Z.; He, Y.; Song, X.; Tan, Z. Titanium dioxide: From engineering to applications. *Catalysts* **2019**, *9*, 191. [CrossRef]

32. Nguyen, T.D.; Li, J.; Lizundia, E.; Niederberger, M.; Hamad, W.Y.; MacLachlan, M.J. Black titania with nanoscale helicity. *Adv. Funct. Mater.* **2019**, *29*, 1904639. [CrossRef]

33. Zhen, D.; Gao, C.; Yang, D.; Zhu, X.; Grimes, C.A.; Liu, Y.; Cai, Q. Blue Ti^{3+} self-doped TiO_2 nanosheets with rich {001} facets for photocatalytic performance. *New J. Chem.* **2019**, *43*, 5759–5765. [CrossRef]

34. Motola, M.; Čaplovičová, M.; Krbal, M.; Sopha, H.; Thirunavukkarasu, G.K.; Gregor, M.; Plesch, G.; Macak, J.M. Ti^{3+} doped anodic single-wall TiO_2 nanotubes as highly efficient photocatalyst. *Electrochim. Acta* **2020**, *331*, 135374. [CrossRef]

35. Yu, X.; Fan, X.; An, L.; Li, Z.; Liu, J. Facile synthesis of Ti^{3+}-TiO_2 mesocrystals for efficient visible-light photocatalysis. *J. Phys. Chem. Solids* **2018**, *119*, 94–99. [CrossRef]

36. Pellegrino, F.; Morra, E.; Mino, L.; Martra, G.; Chiesa, M.; Maurino, V. Surface and Bulk Distribution of Fluorides and Ti^{3+} Species in TiO_2 Nanosheets: Implications on Charge Carrier Dynamics and Photocatalysis. *J. Phys. Chem. C* **2020**, *124*, 3141–3149. [CrossRef]

37. Wang, P.; Jia, C.; Li, J.; Yang, P. Ti^{3+}-doped TiO_2(B)/anatase spheres prepared using thioglycolic acid towards super photocatalysis performance. *J. Alloy. Compd.* **2019**, *780*, 660–670. [CrossRef]

38. Zhao, X.; Guo, K.; Zhang, K.; Duan, S.; Chen, M.; Zhao, N.; Xu, F.J. Orchestrated Yolk-Shell Nanohybrids Regulate Macrophage Polarization and Dendritic Cell Maturation for Oncotherapy with Augmented Antitumor Immunity. *Adv. Mater.* **2022**, *34*, 2108263. [CrossRef]

39. Lei, J.; Zhang, M.; Wang, S.; Deng, L.; Li, D.; Mu, C. One-Pot Approach for the Synthesis of Water-Soluble Anatase TiO_2 Nanoparticle Cluster with Efficient Visible Light Photocatalytic Activity. *J. Phys. Chem. C* **2018**, *122*, 26447–26453. [CrossRef]

40. Mousavi, S.M.; Zarei, M.; Hashemi, S.A.; Ramakrishna, S.; Chiang, W.H.; Lai, C.W.; Gholami, A. Gold nanostars-diagnosis, bioimaging and biomedical applications. *Drug Metab. Rev.* **2020**, *52*, 1–20. [CrossRef]

41. Tian, L.; Feng, H.; Dai, Z.; Zhang, R. Resorufin-based responsive probes for fluorescence and colorimetric analysis. *J. Mater. Chem. B* **2021**, *9*, 53–79. [CrossRef] [PubMed]

42. Dlamini, N.N.; Rajasekhar Pullabhotla, V.S.R.; Revaprasadu, N. Synthesis of triethanolamine (TEA) capped CdSe nanoparticles. *Mater. Lett.* **2011**, *65*, 1283–1286. [CrossRef]

43. Kang, K.-H.; Lee, D.-K. Synthesis of magnesium oxysulfate whiskers using triethanolamine as a morphology control agent. *J. Ind. Eng. Chem.* **2014**, *20*, 2580–2583. [CrossRef]

44. Prakash, T.; Navaneethan, M.; Archana, J.; Ponnusamy, S.; Muthamizhchelvan, C.; Hayakawa, Y. Chemical synthesis of highly size-confined triethylamine-capped TiO_2 nanoparticles and its dye-sensitized solar cell performance. *Bull. Mater. Sci.* **2018**, *41*, 40. [CrossRef]

45. Liu, X.; Gao, S.M.; Xu, H.; Lou, Z.Z.; Wang, W.J.; Huang, B.B.; Dai, Y. Green synthetic approach for Ti^{3+} self-doped TiO$_{2-x}$ nanoparticles with efficient visible light photocatalytic activity. *Nanoscale* **2013**, *5*, 1870–1875. [CrossRef]

46. Wang, X.T.; Li, Y.M.; Liu, X.; Gao, S.M.; Huang, B.B.; Dai, Y. Preparation of Ti^{3+} self-doped TiO$_2$ nanoparticles and their visible light photocatalytic activity. *Chin. J. Catal.* **2015**, *36*, 389–399. [CrossRef]

47. Haque, M.A.; Mahalakshmi, S. Triethanolamine-assisted synthesis of cadmium sulfide nanoclusters. *Res. Chem. Intermed.* **2014**, *41*, 5205–5215. [CrossRef]

48. Du, M.; Yin, X.; Gong, H. Effects of triethanolamine on the morphology and phase of chemically deposited tin sulfide. *Mater. Lett.* **2015**, *152*, 40–44. [CrossRef]

49. Poortavasoly, H.; Montazer, M.; Harifi, T. Aminolysis of polyethylene terephthalate surface along with in situ synthesis and stabilizing ZnO nanoparticles using triethanolamine optimized with response surface methodology. *Mater. Sci. Eng. C Mater. Biol. Appl.* **2016**, *58*, 495–503. [CrossRef]

50. Bai, Q.; Lavenas, M.; Vauriot, L.; Le Trequesser, Q.; Hao, J.; Weill, F.; Delville, J.P.; Delville, M.H. Hydrothermal Transformation of Titanate Scrolled Nanosheets to Anatase over a Wide pH Range and Contribution of Triethanolamine and Oleic Acid to Control the Morphology. *Inorg. Chem.* **2019**, *58*, 2588–2598. [CrossRef]

51. Rezaie, A.B.; Montazer, M. Polyester modification through synthesis of copper nanoparticles in presence of triethanolamine optimized with response surface methodology. *Fibers Polym.* **2017**, *18*, 434–444. [CrossRef]

52. Liang, J.; Li, L.; Luo, M.; Wang, Y. Fabrication of Fe$_3$O$_4$ octahedra by a triethanolamine-assisted hydrothermal process. *Cryst. Res. Technol.* **2011**, *46*, 95–98. [CrossRef]

53. Peng, S.; Dan, M.; Guo, F.; Wang, H.; Li, Y. Template synthesis of ZnIn$_2$S$_4$ for enhanced photocatalytic H$_2$ evolution using triethanolamine as electron donor. *Colloids Surf. A Physicochem. Eng. Asp.* **2016**, *504*, 18–25. [CrossRef]

54. Ramanathan, S.; Moorthy, S.; Ramasundaram, S.; Rajan, H.K.; Vishwanath, S.; Selvinsimpson, S.; Durairaj, A.; Kim, B.; Vasanthkumar, S. Grape seed extract assisted synthesis of dual-functional anatase TiO$_2$ decorated reduced graphene oxide composite for supercapacitor electrode material and visible light photocatalytic degradation of bromophenol blue dye. *ACS Omega* **2021**, *6*, 14734–14747. [CrossRef] [PubMed]

55. Xiong, H.; Wu, L.; Liu, Y.; Gao, T.; Li, K.; Long, Y.; Zhang, R.; Zhang, L.; Qiao, Z.A.; Huo, Q.; et al. Controllable Synthesis of Mesoporous TiO$_2$ Polymorphs with Tunable Crystal Structure for Enhanced Photocatalytic H$_2$ Production. *Adv. Energy Mater.* **2019**, *9*, 1901634. [CrossRef]

56. Yin, G.; Wang, Y.; Yuan, Q. Ti^{3+}-doped TiO$_2$ hollow sphere with mixed phases of anatase and rutile prepared by dual-frequency atmospheric pressure plasma jet. *J. Nanoparticle Res.* **2018**, *20*, 1–12. [CrossRef]

57. Abdullah, S.; Sahdan, M.; Nafarizal, N.; Saim, H.; Embong, Z.; Rohaida, C.C.; Adriyanto, F. Influence of substrate annealing on inducing Ti^{3+} and oxygen vacancy in TiO$_2$ thin films deposited via RF magnetron sputtering. *Appl. Surf. Sci.* **2018**, *462*, 575–582. [CrossRef]

58. Duan, Y.; Grah, P.A.; Cai, F.; Yuan, Z. Enhanced photoelectrochemical performance for hydrogen generation via introducing Ti^{3+} and oxygen vacancies into TiO$_2$ nanorod arrays. *J. Mater. Sci. Mater. Electron.* **2018**, *29*, 20236–20246.

59. Pan, J.; Dong, Z.; Wang, B.; Jiang, Z.; Zhao, C.; Wang, J.; Song, C.; Zheng, Y.; Li, C. The enhancement of photocatalytic hydrogen production via Ti^{3+} self-doping black TiO$_2$/g-C$_3$N$_4$ hollow core-shell nano-heterojunction. *Appl. Catal. B Environ.* **2019**, *242*, 92–99. [CrossRef]

60. Ming, H.; Zhang, H.; Ma, Z.; Huang, H.; Lian, S.; Wei, Y.; Liu, Y.; Kang, Z. Scanning transmission X-ray microscopy, X-ray photoelectron spectroscopy, and cyclic voltammetry study on the enhanced visible photocatalytic mechanism of carbon–TiO$_2$ nanohybrids. *Appl. Surf. Sci.* **2012**, *258*, 3846–3853. [CrossRef]

61. Yu, J.; Wang, B. Effect of calcination temperature on morphology and photoelectrochemical properties of anodized titanium dioxide nanotube arrays. *Appl. Catal. B Environ.* **2010**, *94*, 295–302. [CrossRef]

62. Khan, M.; Ansari, S.; Pradhan, D.; Ansari, M.; Han, D.; Lee, J.; Cho, M. Band gap engineered TiO$_2$ nanoparticles for visible light induced photoelectrochemical and photocatalytic studies. *J. Mater. Chem. A* **2014**, *2*, 637–644. [CrossRef]